An Adaptive Data Processing Framework for Cost-Effective COVID-19 and Pneumonia Detection

Kin Wai Lee
Faculty of Engineering
Universiti Malaysia Sabah
Kota Kinabalu, Malaysia
lee_kin_wai_mk20@iluv.ums.edu.my

Renee Ka Yin Chin
Faculty of Engineering
Universiti Malaysia Sabah
Kota Kinabalu, Malaysia
reneekychin@ums.edu.my

Abstract—**Medical imaging modalities have been showing great potentials for faster and efficient disease transmission control and containment. In the paper, we propose a cost-effective COVID-19 and pneumonia detection framework using CT scans acquired from several hospitals. To this end, we incorporate a novel data processing framework that utilizes 3D and 2D CT scans to diversify the trainable inputs in a resource-limited setting. Moreover, we empirically demonstrate the significance of several data processing schemes for our COVID-19 and pneumonia detection network. Experiment results show that our proposed pneumonia detection network is comparable to other pneumonia detection tasks integrated with imaging modalities, with 93% mean AUC and 85.22% mean accuracy scores on generalized datasets. Additionally, our proposed data processing framework can be easily adapted to other applications of CT modality, especially for cost-effective and resource-limited scenarios, such as breast cancer detection, pulmonary nodules diagnosis, etc.**

Keywords—COVID-19 screening, pneumonia detection, data processing, chest computerized tomography

I. INTRODUCTION

Coronavirus disease (COVID-19) continues spreading in most countries since its emergence in November 2019, affecting 114M people globally at present, with 2.54M deaths (to date March 2, 2021). COVID-19 vaccination has been carried out worldwide since December 2020, with effectiveness varies from 50.38% to 95%. While the vaccination is the ideal solution to control the transmission of the virus, there is real evidence that COVID-19 variants can elude the effectiveness of COVID-19 vaccines [1]. COVID-19 vaccination will be a long journey as new variants continue to emerge. Therefore, there is a desperate need for faster COVID-19 screening alternatives to improve the virus's transmission control.

Medical imaging modalities have been encouraged as a potential alternative to the golden standard current real-time polymerase chain reaction (RT-PCR) test, which suffers long turnaround time and high false-negative rate [2] – [7]. However, large-scale implementation of COVID-19 screening using imaging modalities remains challenging due to three reasons: 1) high invariance radiography representation of ground-glass opacity (GGO) among the viral pneumonia family [4], [5]; 2) limited resources such as data of newly emerged COVID-19 variants ; and 3) practicality of implementation [2]. The advancement of Machine Learning (ML) in recent years has made it possible

for tasks which is difficult or impractical to be implemented previously, especially 3D convolutional neural network for medical applications [5], [8]. Unfortunately, training a 3DCNN model is much complex and exhausting compared to a 2DCNN model. Moreover, 3D training samples with good feature descriptions are exceptionally scarce. Generally, publicly available datasets often suffered from different kind of noises, particularly the non-informative chest CT (NI-CT) slices located at the upper and lower chunk of the 3D CT stacks, which can consequently lead to poor quality model learning [5]. In addition, low contrast, high brightness, and obfuscated CT slices are also among the common CT data-space issues for deep learning applications.

Multiple-source data acquisition can benefit the model development and assessment by offering a wider range of diverse real-world data [4], [5]. However, it can complicate the data processing procedures due to the present of varying data characteristics that might require additional solutions from different data processing tools/algorithms.

This paper presents a cost-effective data processing framework for COVID-19 and pneumonia detection to effectively distinguish COVID-19 and other pneumonia-infected lungs from healthy lungs. Community-acquired pneumonia (CAP) samples and clinical confirmed COVID-19 samples are considered as a single class label in this study due to the invariant radiographic features of GGO that are shared between COVID-19 and CAP CT samples. At the present time, more discriminative multi-class classification task requires further scientific investigation due to the complicated radiography characteristics of COVID-19 and the continuous emergence of new COVID-19 variants.

Three contributions are attributed in this study. Primarily, a wide range of COVID-19, CAP, and healthy chest CT scans are collected, including a mixture of 3D and 2D data types and other varying data characteristics. A data processing framework is proposed to utilize a mixture of 3D and 2D for neural network model development. Finally, the effectiveness of different data processing schemes is demonstrated using quantitative assessment and class activation responses of the models in the COVID-19 and pneumonia detection task.

II. RESOURCES

CT scans of 2419 patients were collected with 1428 COVID-19 cases, 412 community-acquired pneumonia (CAP), and 579 normal lung controls. These CT scans were
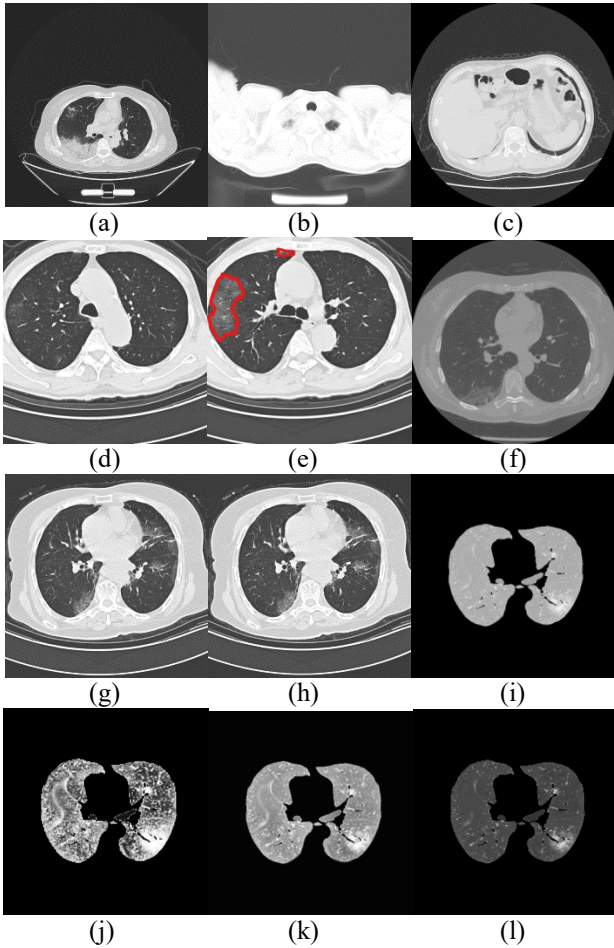
Fig. 1. (a) High-contrast CT, (b) NI-CT slice, (c) small lung regions CT, (d)-(e) CT slices without and with signs of GGO from the same patient. (f) low-contrast CT, (g)-(h) adjacent CT slices which share virtually similar spatial representation, (i) segmented image, (j) image with histogram equalization, (k) CLAHE, (l) supervised gamma adjustment.

contributed by several hospitals, including Union Hospital, Liyuan Hospital in China, Iran Nigen Medical Centre, and several unnamed hospitals in Moscow and China [9] – [11]. The CT data are presented as 3D/2D dimensions, NIfTI/DICOM format, low/high image contrast, Hounsfield/non-Hounsfield unit, and varying image sizes.

III. METHODOLOGY

The complex nature of COVID-19 and pneumonia radiological features can be described based on the formation of GGO and consolidations, which are inconsistent in sizes and locations within the lung regions. Therefore, the probability of a positive true label CT 2D axial slice with absence of pneumonia findings can be high when 3D CT data are decomposed in a 2D system. This scenario is more commonly happened among the early-course infected lung, in which the pneumonia infiltration is barely manifested and hardly visible. Hence, such a data-space condition is defined as ambiguously labeled samples (AL-CT) in this study. It is hypothesized that the utility of AL-CT slices for model

training can complicate the learning process and consequently lead to poor performances as the AL-CT slices share similar spatial representation with the normal lung CT slices.

A. Data Retrieval

The proposed data processing framework provides an end-to-end solution that handles varying data-space issues. In particular, it contains a chain of multiple independent sub-modules that sample the 3D or 2D inputs into a trainable dataset, including 1) NI-CT slices dropout, 2) AL-CT slices dropout, and 3) semi-randomized data generation.

1) NI-CT Slices Dropout

NI-CT slices can be easily identified with visual observation. However, the manual separation of NI-CT slices can be exhaustive when the dataset is large. Therefore, a pretrained model is used to separate the NI-CT slices from the train and test sets based on the sigmoid probability output of the model:

$$P = [p^{ni}, p^{i}] \qquad (1)$$

where p^{ni}, p^{i} represents the sigmoid probabilities corresponding to NI-CT and non-NI-CT respectively. NI-CT slices dropout is performed if $p^{ni} > p^{i}$ for all the 2D CT slices.

2) AL-CT Slices Dropout

The Al-CT slices dropout modules utilizes a binary classifier model that is trained from manually selected normal lung, COVID-19, and CAP infected lung CT images with obvious signs of pneumonia conditions. Subsequently, all positive label CT images are evaluated using the binary classifier for AL-CT detection based on a sigmoid probability p^{a}. High sigmoid probability value p^{a} means a higher likelihood that a CT slice contains signs of pneumonia infiltrations. The dropout decision is based on a threshold value denoted as α. Based on the empirical sigmoid output probability distribution, it is observed that the sigmoid probability for most correctly predicted normal lung CT resides around 0.1. Therefore, α is set to 0.1 with zero as the minimum (no sign of pneumonia findings) and one (very likely to contain pneumonia findings) in the experiment setting. The AL-CT dropout decision can be formulated as follow:

$$outputs = \begin{cases} 0 \ if \ p^{a} < \alpha \\ 1 \ if \ p^{a} >= \alpha \end{cases} \qquad (2)$$

3) Semi-randomized Data Generator Algorithm

The cost-effective property of the proposed framework is defined as a model training environment with comparatively smaller training datasets and neural network model setting compared to existing works [3], [4], [5]. In order to facilitate an end-to-end data generation, an algorithm is proposed to sample CT slices directly from a huge collection of datasets and generate a trainable dataset for model development. CT slices from multi-source datasets are randomly selected for a

Algorithm: Semi-randomized data generator

$Input_{3D} : \{p_i\}_{i=1}^{N_P}$, $\qquad p_i = \{(x_i, y_i)\}_{i=1}^{N=N_q}$

$Input_{2D} : D_{input} = \{(x_i, y_i)\}_{i=1}^{N=N_D}$

$Output : D_t : \{(x_i, y_i)\}_{i=1}^{N_t}$

p = 3D CT of a patient, (x, y) = feature & label pair, N_D = number of 2D CT slices of dataset D, N_P = number of patients, N_q = number of 2D slices in a 3D CT/patient, N_t = number of desired trainable samples.

1: if 3D input:
        randomly select patient p based on $N_{s,3D}$ (desired
        number of patients to be selected)
        while (patients):
2:          standardize dimensions to Nx512x512 pixels
3:          dropout NI-CT slices
4:          randomly select CT slices based on
          $N_{s,3D}$ (desired CT slices from each patient)
5:          compute SSIM
6: return CT slices
7: if 2D input:
8:          standardize data dimension to 512x512 pixels
10:         dropout NI-CT slice
11:         randomly select CT slices based on $N_{s,2D}$, $N_{s,3D}$
         = desired CT slices from a 2D dataset
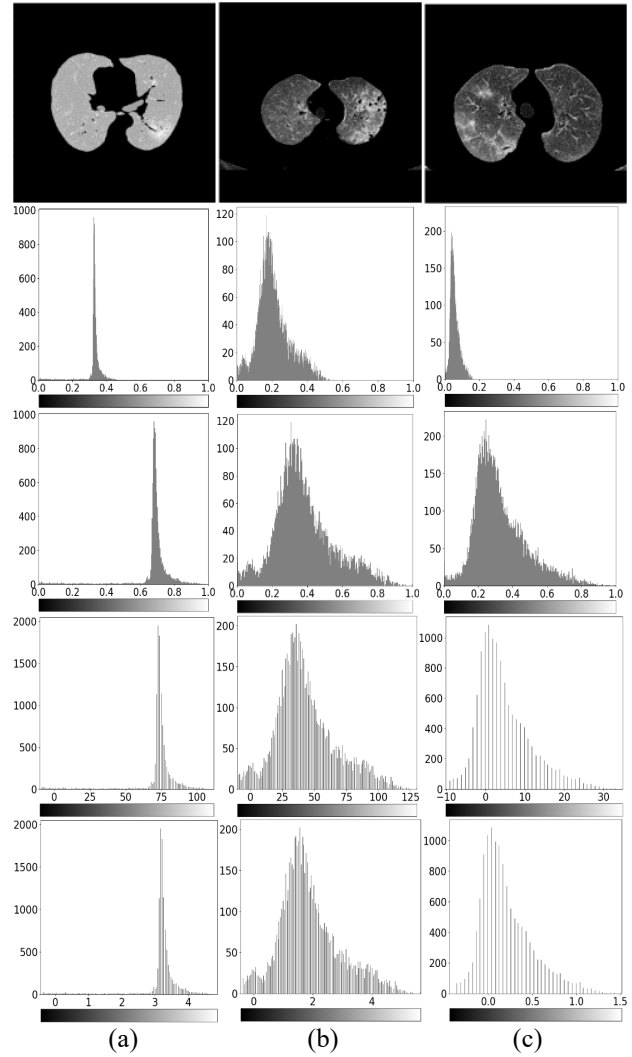12:   compute SSIM
13: return CT slices

Fig. 2. CT image, histogram of unscaled image (2nd row), histogram after normalization (3rd row), centralization (4th row) and standardization (5th row), CT slices are collected from dataset 1 (col (a)), 2 (col (b)) and 3 (col (c)), Note that the background pixels of the images are excluded.

balanced data sampling distribution. Since the number of CT slices acquired from every case (patient) is different, the total number of CT slices retrievable from each dataset is capped to prevent bias data selection towards a particular dataset or patient. The algorithm is considered as semi-randomized due to the exertion of some degree of control over the data selection.

In addition, the proposed algorithm computes the image structural similarity index (SSIM) to identify and separate the adjacent 2D CT slices that are very similar to one another (with SSIM score close to 1). Training with substantial amount of duplicated or closely similar training samples can be fallacious because duplicated samples do not contain additional information that benefits the performance of the model and may consequently suffers overfitting as well as performance degradation, especially in a limited experimental resource setting [12].

B. Lung Segmentation

A simple lung segmentation method is adopted to remove irrelevant information from the lung regions. Different from the deep learning segmentation approaches that require large models and exhaustive training, this method combines several morphological operations and region growing to segment the entire lung regions from the CT background. First, a threshold β is set to identify the foreground (lung regions) and the background (non-lung regions). Pixel higher than β will be assigned with a temporary label L^{temp}. The label assignment proceeds to the neighboring pixels using the

full connected region growing operation until it covers the entire image. Next, the pixel less than β is identified and marked as background label L^b. Finally, L^{temp} and L^b are reassigned to 1s and 0s to create a binary mask for lung segmentation.

C. Image Enhancement and Scaling

Three image enhancement schemes are proposed for image spatial representation improvement, including histogram equalization (HE), contrast limited adaptive histogram equalization (CLAHE), and supervised gamma adjustment (S.GAMMA). HE is the simplest image enhancement technique to improve the image contrast by uniformly redistributing the pixels along the histogram range. CLAHE is generally a better alternative for image enhancement because the redistribution of lightness values happens in a distinctive local region of the image, which

TABLE I.   PERFORMANCE OF COVID-19 AND PNEUMONIA NETWORK TRAINED WITH DIFFERENT DATA PROCESSING SCHEMES

	Train-Validation Set				Test Set			
	ACC.	SEN.	SPE.	AUC.	ACC.	SEN.	SPE.	AUC.
Baseline	82.70±0.96	87.92±3.69	71.99±5.48	92.04±1.11	73.28±3.78	87.52±2.06	48.24±7.52	78.11±3.86
Baseline-SEG	77.75±1.89	89.79±2.46	57.19±7.79	85.37±1.48	56.19±1.74	27.05±3.12	91.00±0.92	65.90±3.51
Baseline-DRP	83.63±1.93	83.28±4.92	83.86±2.87	91.74±1.54	75.61±2 .64	77.89±2.41	73.10±3.04	81.78±2.01
Scale-NOR	82.41±0.99	93.83±2.11	69.09±3.72	93.38±0.65	83.88±1.81	93.05±1.09	73.16±2.26	91.15±1.16
Scale-CTR	79.13±2.34	75.23±5.45	85.26±3.15	87.75±2.81	79.70±2.53	77.19±3.53	82.54±2.69	85.14±2.10
Scale-STD	86.06±0.43	85.70±4.22	86.38±4.18	92.99±0.91	83.93±2.00	86.85±1.68	80.44±2.46	91.15±1.55
HE	75.46±0.49	63.06±2.42	90.47±1.75	87.43±0.82	77.81±2.82	76.50±3.10	79.56±3.32	86.37±2.07
CLAHE	81.40±1.63	83.54±5.58	78.81±5.62	91.70±0.76	84.86±2.47	88.37±2.19	80.80±2.66	91.33±1.08
S.GAMMA	85.66±1.51	89.47±2.32	81.26±4.07	93.42±0.50	85.22±1.88	81.98±2.42	88.98±1.50	92.70±1.11

emphasizing the contrast improvement on the edges from different parts of the image based on an optimized clipped limit to avoid over-enhancement [13]. Images with different lightness and contrast characteristics based on the gamma adjustment transformation graph [14]. For instance, a higher gamma value is used for CT slices with high brightness, low contrast, and a smaller gamma value suitable for images with low brightness.

Image scaling is used to redistribute the pixel values in a fixed pixel range for more efficient model learning [15]. Three most practiced image scaling methods in ML/DL applications are considered in this study: normalization, centralization, and standardization. Normalization is the simplest scaling method to rescale all the images into a range of zero to one [3]. Centralization moves the mean pixel distribution close to zero without considering the range of the pixel distribution. Standardization is an extension of centralization by redistributing the pixels to have standard deviation of one. Figure 2 illustrated CT slices' pixel distributions with different scales.

D. Pneumonia Dectection

The pneumonia detection network is referenced from the VGG16 architecture [16], which composed of a feature extractor with three VGG blocks, a classifier with three fully connected layers, and a sigmoid probability function for the last fully connected layer. The small-scaled model consists of only 40K parameters, which is significantly smaller compared to other existing works: 114M [4], 63.3M [17], 15.9M [5]. Single-channel input CT slices are used for a sequential convolutional operation with ReLU activation and local max-pooling layers in each VGG block and finally output a single channel feature vector using global max-pooling as input for the classifier.

Since it is not the intention of this study to identify the most suitable network architecture for a pneumonia detection application, any DCNN with other architectures is likely to be compatible with the proposed data processing framework with different experimental settings such as larger training set and better computation machines.

E. Training and Validation

The proposed data processing framework generates trainable images with a fix size of 227 x 227 pixels for

computational-efficiency. All the images are augmented using random rotation to minimize overfitting [4]. Based on the reference of the parameter optimization by W. Ning *et al.*, the adative momentum optimizer is used with an initial learning rate of 0.001 and exponential decay rate at 0.9 to improve loss function optimization and model generalization capability [10].

For a better assessment of the detection model's generalization capability, five different test sets are explicitly separated from the train set without overlapping. The train set contains 80% training samples and the remaining 20% as validation samples. Standardized measurements such as accuracy, sensitivity, specificity, and the area under the receiver operator curve (AUC) for quantitative assessment are considered in this study.

IV. RESULTS AND DISCUSSION

The performance of the baseline model trained from the unprocessed raw samples is compared with models trained from datasets that are processed with the different data processing schemes in Table I. Additionally, GradCAM assessment are computed to provide important insights on the models' decision-making behavior and better understand of these responses based on the data processing schemes.

A. Importance of Lung Segmentation

The baseline-SEG model is trained on lung segmented CT images. While the baseline model performed better than the baseline-SEG model based on the performance matrices and ROC curves in figure 3, it is difficult the justify the drastic difference between the two models, particularly, the sensitivity of the Baseline-SEG is at 27.05%, 60.47% lower than the Baseline model. However, the GradCAM demonstrated that the response of Baseline-SEG is intuitively more reasonable despite its poor performance on both Train-Validation and Test Sets. This is because raw images contain a large portion of unrelated information, mainly consist of the bone structures, which are not relevant to any pneumonia or COVID-19 lung infiltration [5], [17], [18]. The GradCAM in Figures 4 (g) and (h) shows that the model's decision-making response includes a huge part of the bone structures, which is not considered a dominant feature of COVID-19 or CAP in the detection task.

B. Learning after AL-CT Dropout

Similar to baseline-SEG model, the baseline-DRP model is trained on lung segmented CT images, but with inclusive of AL-CT slices dropout mechanism. Empirical results show that the Baseline-DRP has a drastic improvement in sensitivity at 77.89% compared to the Baseline-SEG model at 27.05%, while the specificity is slightly dropped on the generalized test sets. This contributed to an overall better-performed model at test accuracy of 75.61%, approximately 20% improvement from the baseline model without AL-CT dropout, shown in the ROC curves. Figure 4 (i) illustrates that the GradCAM response of the baseline-DRP shows a larger area of close attention on the area white pigments than the GradCAM before the AL-CT dropout. This justifies that the AL-CT dropout can effectively disambiguate the confusing feature similarity between the negative label and ambiguous label samples and contributed to a more discriminative feature learning between positive and negative label samples. For all the subsequent experiments, the AL-CT dropout mechanism is equipped as one of the pre-requisite data processing procedures together with lung segmentation.

C. Learning with Scaled Datasets

The impact of the image scaling is more significantly illustrated on the generalized dataset compared to the test-validation performance by the models. For instance, the normalization Scale-NOR model on the test sets shows superior performance in terms of accuracy score (83.88%) compared to the unscaled Baseline-DRP model (75.61%) and centralization Scale-CTR model (79.70%), and at the same time on par with standardization Scale-STD model (83.93%). Figure 4 (b) demonstrates the impact of scaling on the model's attention responses, in which the attention coverage is more precisely annotated on the pneumonia infiltrations. Thus, this proves that a more reliable model can be trained from a scaled image with a more homogeneous pixel distribution between training samples from different sources. In essence, image scaling by normalization is considered as the most effective scaling method in the experimental settings for simplicity and good performance.
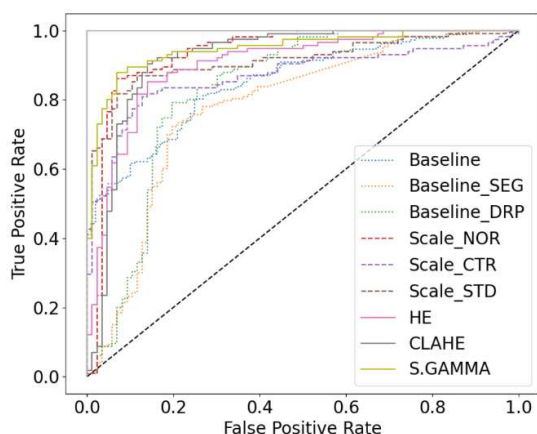

Fig. 3. ROC of COVID-19 and pneumonia network trained with different data processing schemes on a test sets.

D. Effectivenss of Image Ehancement Schemes

Overall, supervised gamma adjustment has the highest contribution on both train-validation sets and test sets, which yielded the overall highest model pneumonia detection model performances in the experiments at test accuracy of 85.22% with 11.94%, 29.03%, and 9.61% improvements from the Baseline, Baseline-SEG, and Baseline-DRP models, respectively. This result is comparable to other existing pneumonia detections with more complex experimental settings [3], [4]. It is also noticed that the difference in model performances between the supervised gamma adjustment and the standard CLAHE is not significant on generalized datasets, this suggests that image enhancements have a relatively smaller contribution compared to other data-processing procedures in the experimental settings of this study. Nevertheless, the ROC in figure 3 shows significant differences between the models trained with enhanced dataset and the baseline models. This highlighted the importance of the proposed data processing procedures for pneumonia detection networks.

On the contrary, HE suffers significantly poor performances and the GradCAM assessment indicates the common over-enhancement drawback of the standard HE, as shown in figure 4 (c). It is observed that the non-pneumonia lesion on the left side of the lung is falsely perceived by the model, which can be considered a sign of image distortion due to over-enhancement [13]. The CLAHE has a relatively higher sensitivity, which is concordant to its GradCAM response shown in figure 4 (d) with weak attention on the pneumonia infiltrations. On the other hand, the S.GAMMA model achieves high specificity with a relatively lower sensitivity compared to CLAHE, which is illustrated by the more accurate GradCAM responses compared to other models.

V. CONCLUSION

This paper presents a cost-effective detection model to efficiently distinguish CAP and COVID-19 using CT imaging to reduce the risk of COVID-19 being transmitted to the healthy community. Important insights of the end-to-end data processing pipeline for CT-based COVID-19 and pneumonia detection are revealed. Primarily, the significance of lung segmentation is justified based on improved class activation annotation of the model trained from lung segmented datasets. In addition, the data-space problem of NI-CT and AL-CT are clearly identified and addressed using a strategic data dropout approach without sacrificing the diversity of the data. To this end, empirical results demonstrate significant performance improvement due to the disambiguation of the similar spatial representations that are shared between the normal and COVID-19 infected lung CT images. Moreover, image scaling and enhancement are deduced as crucial pre-requisite data processing for image-based deep learning applications, especially when involving different data resources. As such, the proposed data processing framework facilitated a cost-effective with promising performance COVID-19 and pneumonia detection without utilizing any computationally expensive approaches such as 3D image modelling or very deep neural networks.
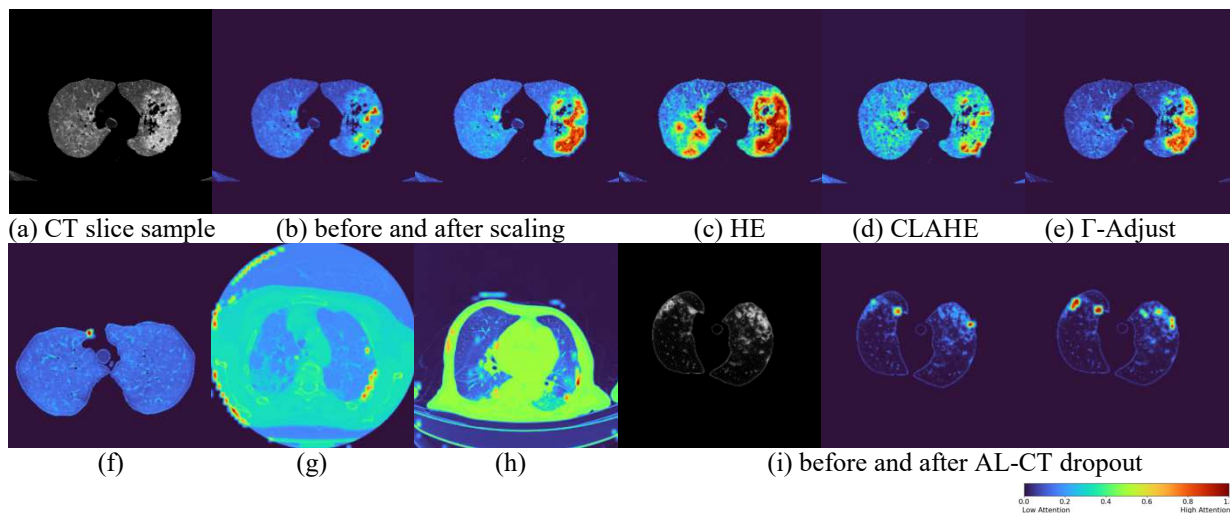
Fig. 4. (a) a COVID-19 infected CT slice, (b) GradCAM before and after global datasets scaling, (c) – (e) GradCAM of the models trained from datasets enhanced with global histogram equaliztion, CLAHE and supervised gamma adjustement, (f) low attention GradCAM response of a health lung, (g) – (h) GradCAM of unsegmented COVID-19 and CAP, (i) a COVID-19 CT slice and GradCAM before and after the porposed AL-CT dropout.

It is worth mentioning that the data processing framework can be extended easily to different medical ML/DL applications, especially in attempts of utilizing 3D data in a 2D-based solution. That is, it can be referenced as data pre-processing procedures for relatable applications to improve data diversity and quality for more efficient neural network development in a cost-effective setting.

VI. ACKNOWLEDGEMENT

REFERENCES

[1] I. S. Africa and I. Brazil, "COVID-19 New Variants of the Virus that Causes COVID-19 What it means," no. January, pp. 1–2, 2021.

[2] G. D. Rubin et al., "The Role of Chest Imaging in Patient Management during the COVID-19 Pandemic: A Multinational Consensus Statement from the Fleischner Society," Radiology, vol. 296, no. 1, pp. 172–180, Jul. 2020, doi: 10.1148/radiol.2020201365.

[3] J. Zhang et al., "Viral Pneumonia Screening on Chest X-rays Using Confidence-Aware Anomaly Detection," IEEE Trans. Med. Imaging, pp. 1–1, 2020, doi: 10.1109/tmi.2020.3040950.

[4] M. J. Horry et al., "COVID-19 Detection through Transfer Learning Using Multimodal Imaging Data," IEEE Access, vol. 8, pp. 149808–149824, 2020, doi: 10.1109/ACCESS.2020.3016780.

[5] J. Wang et al., "Prior-Attention Residual Learning for More Discriminative COVID-19 Screening in CT Images," IEEE Trans. Med. Imaging, vol. 39, no. 8, pp. 2572–2583, 2020, doi: 10.1109/TMI.2020.2994908.

[6] Y. Li and L. Xia, "Coronavirus disease 2019 (COVID-19): Role of chest CT in diagnosis and management," Am. J. Roentgenol., vol. 214, no. 6, pp. 1280–1286, 2020, doi: 10.2214/AJR.20.22954.

[7] W. Zhao, Z. Zhong, X. Xie, Q. Yu, and J. Liu, "Relation between chest CT findings and clinical conditions of coronavirus disease (covid-19) pneumonia: A multicenter study," Am. J. Roentgenol., vol. 214, no. 5, pp. 1072–1077, 2020, doi: 10.2214/AJR.20.22976.

[8] M. Liu, D. Cheng, and W. Yan, "Classification of alzheimer's disease by combination of convolutional and recurrent neural networks using FDG-PET images," Front. Neuroinform., vol. 12, no. June, pp. 1–12, 2018, doi: 10.3389/fninf.2018.00035.

[9] S. P. Morozov et al., "MosMedData: Chest CT Scans With COVID-19 Related Findings Dataset," arXiv, May 2020, [Online]. Available: http://arxiv.org/abs/2005.06465.

[10] W. Ning et al., "Open resource of clinical data from patients with pneumonia for the prediction of COVID-19 outcomes via deep learning," Nat. Biomed. Eng., vol. 4, no. 12, pp. 1197–1207, 2020, doi: 10.1038/s41551-020-00633-5.

[11] T. Yan, P. K. Wong, H. Ren, H. Wang, J. Wang, and Y. Li, "Automatic distinction between COVID-19 and common pneumonia using multi-scale convolutional neural network on chest CT scans," Chaos, Solitons and Fractals, vol. 140, p. 110153, 2020, doi: 10.1016/j.chaos.2020.110153.

[12] K. W. Lee and R. K. Y. Chin, "The Effectiveness of Data Augmentation for Melanoma Skin Cancer Prediction Using Convolutional Neural Networks," in 2020 IEEE 2nd International Conference on Artificial Intelligence in Engineering and Technology (IICAIET), Sep. 2020, pp. 1–6, doi: 10.1109/IICAIET49801.2020.9257859.

[13] Z. Ullah, M. U. Farooq, S. H. Lee, and D. An, "A hybrid image enhancement based brain MRI images classification technique," Med. Hypotheses, vol. 143, no. April, p. 109922, 2020, doi: 10.1016/j.mehy.2020.109922.

[14] S. Rahman, M. M. Rahman, M. Abdullah-Al-Wadud, G. D. Al-Quaderi, and M. Shoyaib, "An adaptive gamma correction for image enhancement," Eurasip J. Image Video Process., vol. 2016, no. 1, pp. 1–13, 2016, doi: 10.1186/s13640-016-0138-1.

[15] S. Ren, K. He, R. Girshick, and J. Sun, "Faster R-CNN: Towards Real-Time Object Detection with Region Proposal Networks," IEEE Trans. Pattern Anal. Mach. Intell., vol. 39, no. 6, pp. 1137–1149, 2017, doi: 10.1109/TPAMI.2016.2577031.

[16] K. Simonyan and A. Zisserman, "Very deep convolutional networks for large-scale image recognition," 3rd Int. Conf. Learn. Represent. ICLR 2015 - Conf. Track Proc., pp. 1–14, 2015.

[17] X. Ouyang et al., "Dual-Sampling Attention Network for Diagnosis of COVID-19 From Community Acquired Pneumonia," IEEE Trans. Med. Imaging, vol. 39, no. 8, pp. 2595–2605, Aug. 2020, doi: 10.1109/TMI.2020.2995508.

[18] F. Shi et al., "Large-scale screening of COVID-19 from community acquired pneumonia using infection size-aware classification," Phys. Med. Biol., Feb. 2021, doi: 10.1088/1361-6560/abe838.